Online Research @ Cardiff

Citation for final published version:

information services
gwasanaethau gwybodaeth

G-quadruplex organic frameworks

Yi-Lin Wu[1,2]*, Noah E. Horwitz[1], Kan-Sheng Chen[3], Diego A. Gomez-Gualdron[4†], Norman S. Luu[3], Lin Ma[1,2], Timothy C. Wang[1], Mark C. Hersam[1,2,3], Joseph T. Hupp[1,2], Omar K. Farha[1,5], Randall Q. Snurr[4] and Michael R. Wasielewski[1,2]*

Two-dimensional covalent organic frameworks often π stack into crystalline solids that allow precise spatial positioning of molecular building blocks. Inspired by the hydrogen-bonded G-quadruplexes found frequently in guanine-rich DNA, here we show that this structural motif can be exploited to guide the self-assembly of naphthalene diimide and perylene diimide electron acceptors end-capped with two guanine electron donors into crystalline G-quadruplex-based organic frameworks, wherein the electron donors and acceptors form ordered, segregated π-stacked arrays. Time-resolved optical and electron paramagnetic resonance spectroscopies show that photogenerated holes and electrons in the frameworks have long lifetimes and display recombination kinetics typical of dissociated charge carriers. Moreover, the reduced acceptors form polarons in which the electron is shared over several molecules. The G-quadruplex frameworks also demonstrate potential as cathode materials in Li-ion batteries because of the favourable electron- and Li-ion-transporting capacity provided by the ordered rylene diimide arrays and G-quadruplex structures, respectively.

Charge transport through self-assembled arrays of π-stacked molecules is a key process in organic electronics. This trans-port is expected to be efficient when the molecules are in close π contact, which provides large intermolecular electronic coupling[1,2]. To reveal the mechanism of charge generation and transport in this architecture, we and others have examined self-assembled donor–acceptor (DA) molecules that form segregated donor and/or acceptor (D/A) domains in solution or in the solid state, and have found evidence for charge sharing and efficient carrier migration within these supramolecular structures[3–5]. As charge-transport efficiency is greatly influenced by the molecular ordering of π-stacked D/A domains, the periodic molecular arrays of crystalline two-dimensional covalent organic frameworks (2D COFs)[6–9] developed in recent years offer a promising scaffold to enhance the performance of organic (semi)conductive materials. Indeed, significant electrical conductivity, photoconductivity with large on–off ratios and long-lived photogenerated charge carriers have been reported for pyrene-, triphenylene-, porphyrin- and phthalocyanine-based 2D COFs[10–14].

Owing to the strong association between molecules forming arrays of multipoint hydrogen bonds ($K_a \sim 10^{5–12}$ M^{-1}) (ref. 15), non-covalent frameworks that exploit hydrogen bonding have attracted increasing attention[16–18]. The planar geometry of multiply hydrogen-bonded arrays is suitable for generating 2D architectures. This methodology is different from conventional assembly methods, in which the 2D framework is constructed using reversible covalent linkages of boronate ester, imine or triazine functionalities[6–9]. Based on our previous experience with self-ordering G-quadruplex-based DA assemblies[19,20], we reason that the π-stacking properties of the G-quadruplex, together with its hydrogen-bond forming ability, can be exploited for organic framework synthesis.

Specifically, a 2D framework with tetragonal grids can be assembled from linear molecules end-capped with two guanines to form G-quartets with the neighbouring guanines via Hoogsteen hydrogen bonds (Fig. 1). The groups of Besenbacher and Sessler have observed the formation of cation-free G-quartets on the Au (111) surface and in a single crystal, respectively[21,22]. Stacking of the 2D sheets to yield the G-quadruplex-based organic framework is realized by π–π interactions between G-quartets and between polycyclic aromatic chromophores. Importantly, the π stacking of G-quadruplexes constrains donors and acceptors to segregated columns and minimizes mixed stacking that may lead to deleterious recombination sites for photogenerated charge carriers.

With this expectation, we designed two DA G-quadruplex 2D frameworks composed of the electron-rich G-quartet, which acts as the electron donor, and the strongly electron-accepting naphtha-lene-1,4:5,8-bis(dicarboximide) (in NDI) or 2,5,8,11-tetrahexylpery-lene-3,4:9,10-bis(dicarboximide) (in PDI, see Fig. 1). These chromophoric units are devoid of functional groups that interfere with the G-quadruplex hydrogen-bond formation, and their extended planar π surfaces facilitate close stacking between the 2D layers.

Results and discussion

Framework formation and structural characterization. A strategy that employs the hydrogen-bond blocking tert-butyloxycarbonyl (Boc) protecting group was used to allow the handling and purification of bis(guanine) derivatives[16,23], Boc_6G_2NDI and Boc_6G_2PDI, which were prepared via Sonogashira coupling between bis-ethynylated rylene diimides (E_2NDI and E_2PDI) and fully Boc-protected N^9-octyl guanine (Boc_3GBr) (Fig. 1). n-Hexyl substituents were introduced on PDI at the 2, 5, 8 and 11 positions to ensure the solubility of the synthetic intermediates; these substituents have minimal impact on the PDI structural planarity[24].

The formation of the G_2NDI and G_2PDI frameworks was effected by first removing the Boc groups with trifluoroacetic acid (TFA) in CH_2Cl_2, followed by vapour exchange between

[1]Department of Chemistry, Northwestern University, Evanston, Illinois 60208, USA. [2] Argonne–Northwestern Solar Energy Research (ANSER) Center, Northwestern University, Evanston, Illinois 60208, USA. [3] Department of Materials Science and Engineering, Northwestern University, Evanston, Illinois 60208, USA. [4] Department of Chemical and Biological Engineering, Northwestern University, Evanston, Illinois 60208, USA. [5] Department of Chemistry, Faculty of Science, King Abdulaziz University, Jeddah 22254, Saudi Arabia. [†]Present address: Department of Chemical and Biological Engineering, Colorado School of Mines, Golden, Colorado 80401, USA. *e-mail: yi-lin.wu@northwestern.edu; m-wasielewski@northwestern.edu
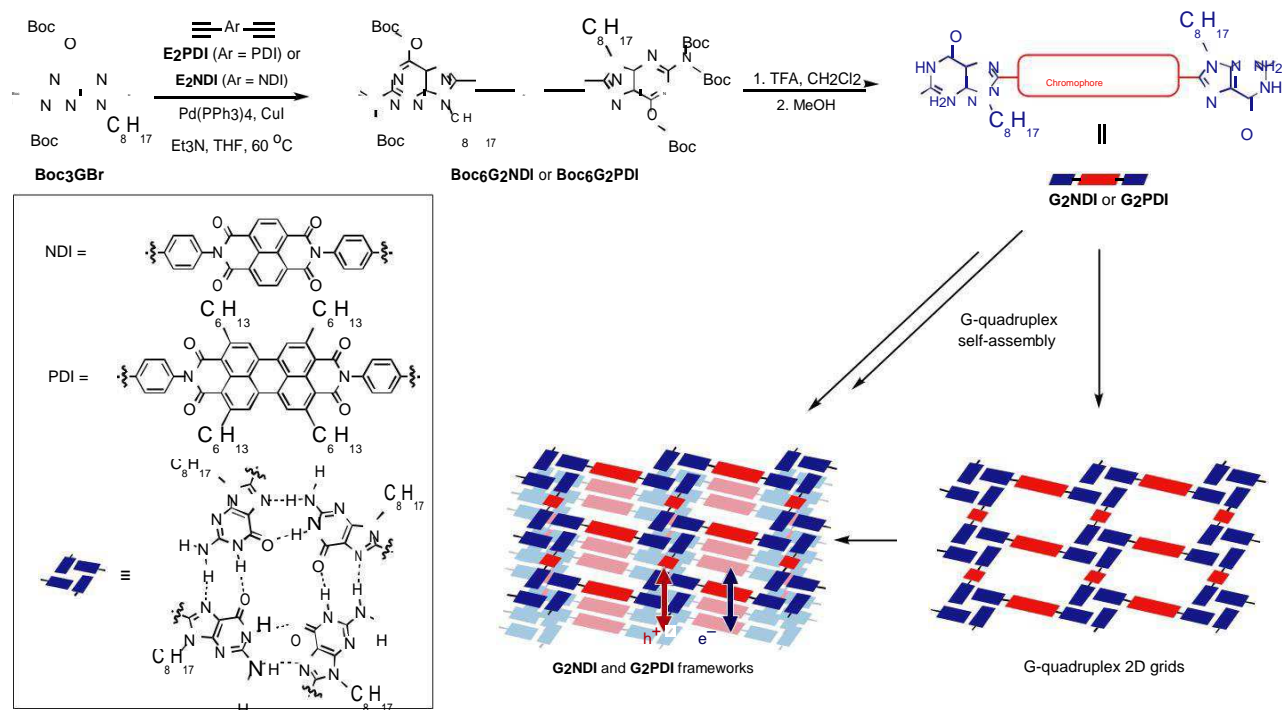
Figure 1 | Preparation of G-quadruplex organic frameworks. The construction of G-quadruplex organic frameworks through a two-step process that consists of a cross-coupling reaction (3–4 equiv. of Boc3GBr with Pd(PPh3)4/CuI catalysts, 43–50% yield) and protecting group removal (CF3CO2H in CH2Cl2, followed by vapour exchange with MeOH for slow crystallization, quantitative). The ordered π stacks of chromophores offer segregated conduits for hole and electron transport. Boc = tert-butyloxycarbonyl, THF = tetrahydrofuran, TFA = CF3COOH.
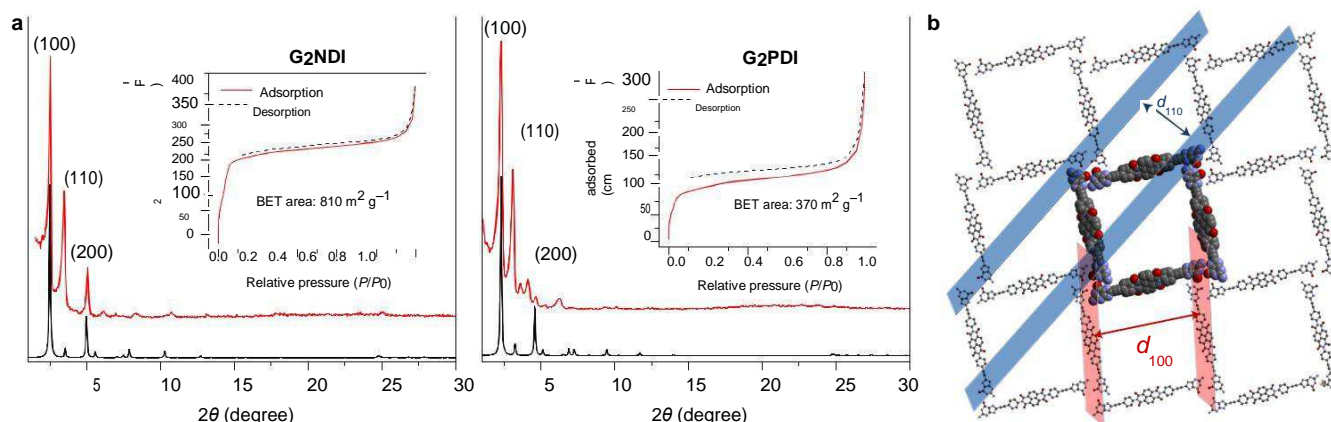

Figure 2 | Crystalline and porous G-quadruplex organic frameworks of G2NDI and G2PDI. a, Red trace, observed powder X-ray diffraction patterns; black trace, simulated ones. The insets show the N2-adsorption isotherm. b, One layer of simulated G-quadruplex framework structures. The (100) and (110) diffraction planes are shown. STP, standard temperature and pressure.

TFA/CH2Cl2 and MeOH in a sealed chamber at room temperature. The molecular structure and purity of G2NDI and G2PDI were determined by ^1H and ^{13}C NMR spectroscopy in CD2Cl2 (with 4% TFA) or (CD3)2SO (for G2NDI) and high-resolution mass spectrometry (Supplementary Section 2). The crystallites of G2NDI and G2PDI display a rod-like morphology, and hydrogen bonding in these materials was evident by the observation of a new carbonyl-stretching band at ~1,678 cm^{-1} by Fourier transform infrared spectroscopy (Supplementary Sections 3 and 4). The frameworks are insoluble in common organic solvents with low-to-medium–high polarity; however, G2NDI is slightly soluble in (CH3)2SO and N,N-dimethylformamide (DMF), and the latter solvent was found useful to improve the crystallinity of G2PDI (insoluble in DMF; 50 °C for five days). The G2PDI framework displays a high degree

of thermogravimetric stability up to 350 °C, whereas about 16% of the weight loss was observed at 130 °C for the G2NDI sample (Supplementary Section 5).

The G2NDI framework displays a high degree of crystallinity based on its powder X-ray diffraction pattern (PXRD), which shows distinct diffraction peaks at 2.55°, 3.45° and 5.10° (Cu Kα (Fig. 2)). On the other hand, DMF-annealed G2PDI shows diffrac-tion peaks at 2.25° and 3.14°. The d spacing that corresponds to the lowest-angle diffraction peaks correlates well to the molecular size measured from one NH2 to the other NH2 groups (35.0 and 39.2 Å for G2NDI and G2PDI, respectively), and that for the second diffraction peak is equal to √2/2 of the previous value. Such a diffraction pattern is consistent with 2D frameworks constructed from tetragonal grids with molecular G2NDI or G2PDI as the
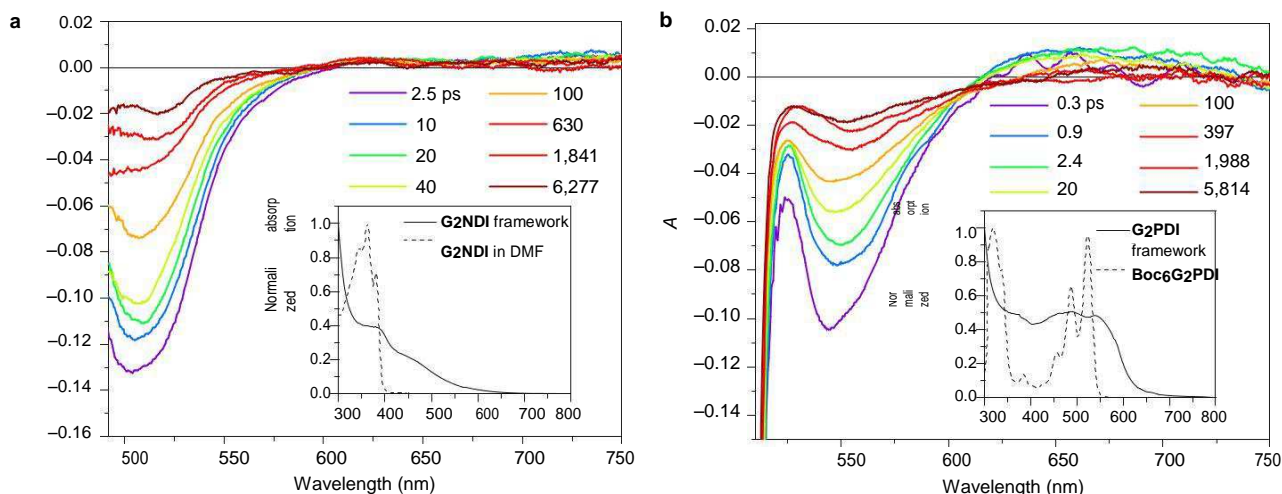
Figure 3 | Femtosecond time-resolved transient-absorption spectra. a,b, Transient absorption spectra of G$_2$NDI (a) and G$_2$PDI (b) frameworks recorded at time delays indicated in the legends after laser excitation. The solid samples were fixed in a polyisobutylene matrix at room temperature. The insets show the ground-state absorption spectra of the G$_2$NDI and G$_2$PDI monomers and frameworks.

side of each tetragon. The observation of moderate N$_2$ adsorption (Brunauer–Emmett–Teller areas of 810 and 370 m^2 g^{-1} for G$_2$NDI and G$_2$PDI, respectively) further supports the microporous superstructure. The lower N$_2$ uptake for G$_2$PDI relative to G$_2$NDI partially results from the presence of n-hexyl side chains in the pore[25].

The proposed G-quadruplex framework structure is further supported by the simulated PXRD patterns (Fig. 2 and Supplementary Section 6), which are based on the AA-stacked 2D grids of G-quadruplexes, and the most distinct diffraction peaks at low angles were assigned to the (100), (110) and (200) facets. A few other possible self-assembled solid-state structures based on hydrogen-bonded guanine association were considered, including significantly slip-stacked G-quadruplexes (AB stack) and guanine ribbons[26,27]; however, the mismatch between the simulated PXRD patterns and the experimentally observed ones exclude the presence of significant amounts of these alternative structures. The superior N$_2$ uptake of the G$_2$NDI framework, relative to G$_2$PDI, was similarly found in the simulated N$_2$ isotherms for the two structures (Supplementary Section 6). An analysis of pore-size distribution is provided in Supplementary Section 7.

Optical properties and charge-transport dynamics. Cofacial stacking of NDI and PDI in the respective G$_2$NDI and G$_2$PDI frameworks results in broad, red-shifted absorption in the visible region compared with the spectra of the corresponding monomers in solution (Fig. 3, insets). Given the crystallinity of the G$_2$NDI and G$_2$PDI frameworks and the similarity of their absorption spectra to those of an NDI-based cyclophane[28] and alkyl-substituted PDI thin films[4], respectively, this shift is attributed to a combination of excitonic coupling and charge-transfer (CT) interactions between the closely π-stacked chromophores. In another instance, a similar absorption was found for an NDI-based metal organic framework[29], the colour of which was believed to result primarily from CT interactions.

The excited-state energies of ^{1*}NDI and ^{1*}PDI are E_S = 3.22 (ref. 30) and 2.35 eV (ref. 31), respectively, the one-electron oxidation potential of phenylethynyl guanine is E_{ox} = 1.1 V versus the saturated calomel electrode (SCE)[19] and the one-electron reduction potentials of NDI and PDI are E_{red} = −0.5 (ref. 32) and −0.75 V (ref. 31) versus SCE, respectively. The data given above and the Weller equation[33] were used to estimate the free energies for G−^{1*}NDI → G$^{\bullet+}$−NDI$^{\bullet-}$ (G_{CS} = −1.3 eV (CS, charge separation)) and for G−^{1*}PDI → G$^{\bullet+}$−PDI$^{\bullet-}$ (G_{CS} = −0.2 eV), which should

lead to the facile formation of holes and electrons that can be trans-ported along the stacks of the G-quadruplexes and NDI or PDI, respectively (Supplementary Section 8).

Irradiation of G$_2$NDI and G$_2$PDI with low-fluence laser pulses (20 nJ, 150 fs) at 400 and 500 nm, respectively, resulted in ultrafast charge transfers within the instrument response (150 fs) to form long-lived G$^{\bullet+}$−NDI$^{\bullet-}$ and G$^{\bullet+}$−PDI$^{\bullet-}$ radical ion pairs (polaron pairs) in the frameworks. Thus, the charge-separation reactions occur much faster than the corresponding decay times of the lowest excited singlet state of ^{1*}NDI (τ_{S1} = 2 ps) (ref. 30) and ^{1*}PDI (τ_{S1} = 4.5 ns) (ref. 31), which results in nearly quantitative yields of radical ion pairs. The time-resolved absorption spectra shown in Fig. 3 are dominated by the ground-state bleach signals, which for G$_2$NDI cancel out the 480 nm band charac-teristic of NDI$^{\bullet-}$ (ref. 32). For G$_2$PDI, the near-infrared band at 700 nm usually observed for PDI$^{\bullet-}$ is substantially broadened, as we have observed previously in π-stacked PDI derivatives[3,4,19]. In each case, the transient kinetics are fit to two fast charge-recombina-tion processes and a much slower one (Supplementary Section 9). The two fast processes are assigned to geminate recombination of G$^{\bullet+}$−NDI$^{\bullet-}$ (τ_{CR1} = 8.6 ps (21%); τ_{CR2} = 106 ps (44%) (CR, charge recombination) and G$^{\bullet+}$−PDI$^{\bullet-}$ (τ_{CR1} = 1.4 ps (31%); τ_{CR2} = 88 ps (39%)). The slow process that occurs on the microsecond timescale represents 35 and 30% of the amplitude of the decay of G$^{\bullet+}$− NDI$^{\bullet-}$ and G$^{\bullet+}$−PDI$^{\bullet-}$, respectively, and is assigned to the recombina-tion of free carriers, as discussed below. This type of kinetic behav-iour is often observed in organic bulk heterojunction solar cells[34,35].

The long-lived, photogenerated radical ion pairs were further characterized using time-resolved electron paramagnetic resonance (TREPR) spectroscopy. The TREPR spectra of G$^{\bullet+}$−NDI$^{\bullet-}$ and G$^{\bullet+}$− PDI$^{\bullet-}$ shown in Fig. 4a were measured at 100 ns after a 416 nm or 500 nm, respectively, laser pulse of 7 ns using direct microwave detection (Supplementary Section 10). The TREPR spectra are spin polarized because of their formation mechanism described below; thus, positive signals indicate an enhanced absorption of microwave energy and negative signals denote emission. The spectra of both G$^{\bullet+}$−NDI$^{\bullet-}$ and G$^{\bullet+}$−PDI$^{\bullet-}$ are completely emissive at the X band (9.5 GHz (Supplementary Section 10 gives the time evolution of the spectra)). The narrow width (~3 mT) of the TREPR spectra indicates that the primary photogenerated transient species are radical ion pairs, rather than the neutral excited triplet states of NDI[36] or PDI[37] (usually ~100 mT wide), which supports the assignments in the transient-absorption experiments.
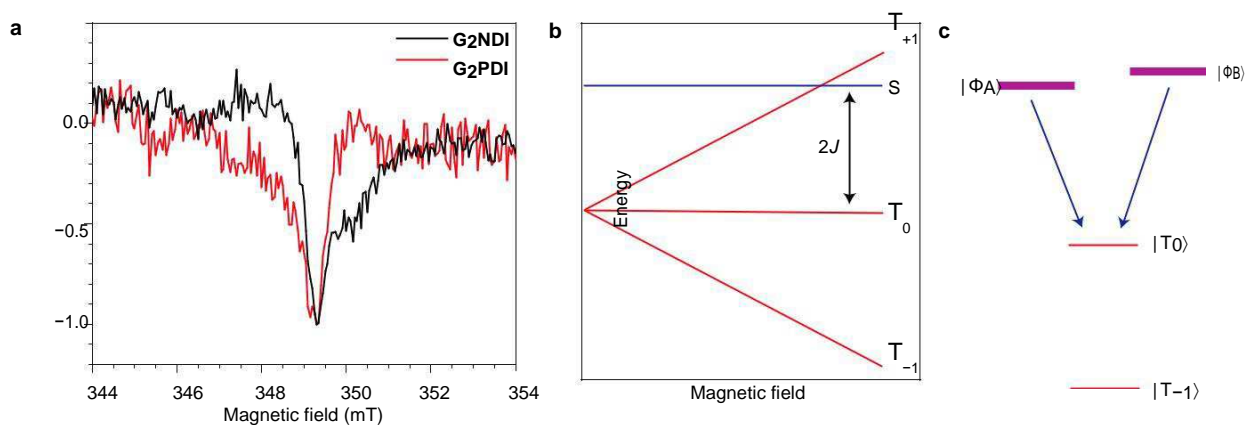
Figure 4 | Time-resolved EPR spectra. a, The spin-polarized X-band EPR signals of radical ion pairs generated in G2NDI and G2PDI at 295 K and 100 ns after photoexcitation using a 416 nm or 500 nm, respectively, laser pulse of 7 ns. b, Zeeman splitting of the radical ion pair spin-energy levels (2J > 0), where 2J (spin–spin exchange interaction) depicts a large S–T energy splitting, S is the singlet state of the radical pair and T_{+1}, T_0 and T_{-1} are the triplet sublevels split by the Zeeman interaction in the high magnetic field limit. c, Radical pair energy levels and transitions in the high magnetic field limit after $S–T_{+1}$ mixing to yield Φ_A and Φ_B, which initially are populated. The arrows indicate the microwave-induced transitions responsible for the observed spin-polarized TREPR spectra.
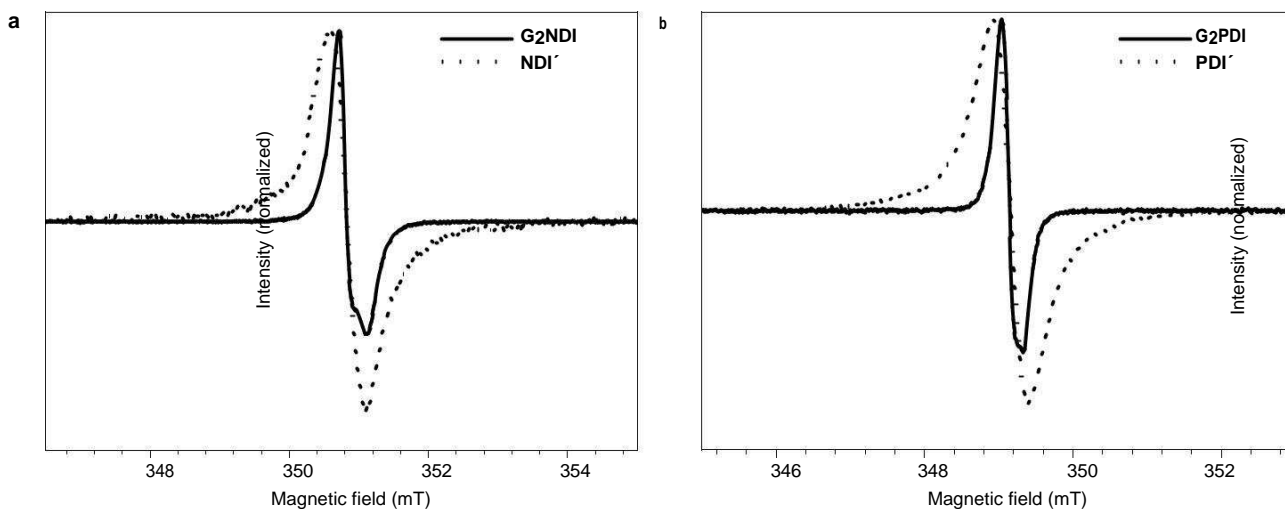

Figure 5 | Comparison of CW-EPR spectra of reduced rylene diimides in the frameworks and in isolated molecules. a,b, Solid lines: EPR signal of partially reduced G2NDI (a) and G2PDI (b) frameworks at 295 K (CoCp2 reductant). Dotted lines: the spectra of the anions of monomeric model NDI′ (a) and PDI′ (b), where NDI′ is N,N-bis(2,5-di-tert-butylphenyl)naphthalene-1,4:5,8-bis(dicarboximide) and PDI′ is N,N-bis(4-(triisopropylsilylethynylphenyl)-2,5,8,11-tetrahexylperylene-3,4:9,10-bis(dicarboximide).

The TREPR spectra can be explained by considering the spin–spin interactions of the two radicals that comprise the radical ion pair. If photodriven charge separation within an organic DA system occurs in ≪1 ns, the spin state of the initially formed singlet or triplet excited donor or acceptor is carried over to the corresponding singlet or triplet radical ion pair, $^1(D^{•+}–A^{•-})$ or $^3(D^{•+}–A^{•-})$, respectively, which may then interconvert by the radical-pair intersystem crossing mechanism[38]. The isotropic spin–spin exchange interaction (2J), which depends exponentially on distance, splits the singlet and triplet manifolds (Fig. 4b). For radical ion pairs having large negative free energies of charge recom-bination, such as $G^{•+}–NDI^{•-}$ and $G^{•+}–PDI^{•-}$, where recombination occurs in the Marcus inverted region of the rate versus free-energy dependence, it has been shown that 2J > 0, which places the singlet energy level above those of the triplet sublevels at zero magnetic field using the sign convention typical of TREPR spectroscopy[3,4,20,39].

At the $B_0 = 350$ mT magnetic field used for TREPR spectroscopy at 9.5 GHz, the $^3(D^{•+}–A^{•-})$ triplet sublevels are split by the Zeeman interaction, and are described by the T_{+1}, T_0 and T_{-1} states quantized along the field, whereas the $^1(D^{•+}–A^{•-})$ energy level (S) remains field invariant (Fig. 4b)[38]. When the radical ion pair distance is ~10–20 Å, 2J is sufficiently large that $S–T_{+1}$ mixing occurs to produce states $|\Phi_A\rangle$ and $|\Phi_B\rangle$ (Fig. 4c). Given that charge separation within G2NDI and G2PDI takes place from their respective lowest excited singlet states, initially $|\Phi_A\rangle$ and $|\Phi_B\rangle$ are populated, so that microwave-induced transitions between these states and the unpopulated $|T_0\rangle$ state result in an all-emissive spin-polarized EPR spectrum in the early period[38]. To test this model, TREPR experiments were also performed at higher magnetic field (Q band, 34 GHz) to increase the energy of the $|T_{+1}\rangle$ state, and thereby decrease $S–T_{+1}$ mixing and increase $S–T_0$ mixing; these results are presented in Supplementary Section 10. In contrast to the results at 9.5 GHz, both emissive and absorptive transitions are observed for G2NDI and G2PDI, which shows predominant $S–T_0$ mixing at this field. Taken together, these results are consistent with either an intermediate value or a large
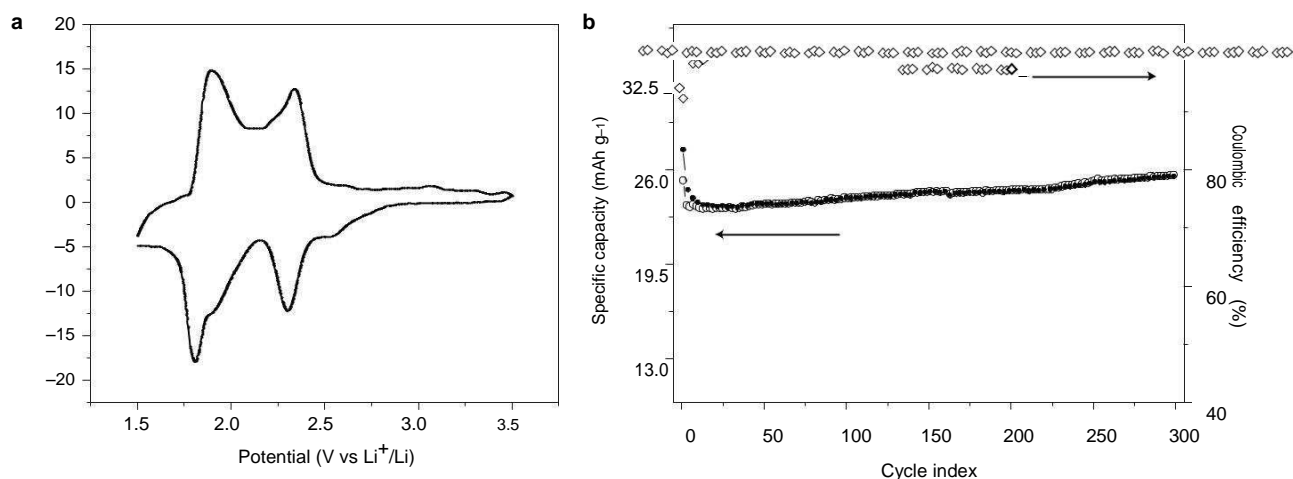
Figure 6 | Electrochemical response and performance of a Li-ion battery using G2PDI as the cathode. a, Cyclic voltammogram of the G2PDI battery scanned at 0.5 mV s^{-1}. b, Galvanostatic charge/discharge cycling of a G2PDI battery tested for 300 cycles. The specific charge and discharge capacity are shown as solid and hollow circles, respectively, and the coulombic efficiency is shown as hollow diamonds.

distribution of 2J during the mixing time. Alternatively, S−T$_{+1}$ mixing may occur during diffusional encounters of charge carriers, which results in briefly increased 2J (ref. 40).

This spin–spin interaction provides a time window for observing the radical ion pairs over the first 1–2 µs of their lifetime prior to the formation of free charge carriers. During this time the radical ions that comprise the radical ion pair are sufficiently close (~10–20 Å) to remain strongly spin coupled, so that if they are moving within the framework structure on this timescale, they must necessarily move in concert to maintain spin correlation.

We probed the next stage in the time evolution of the photogenerated long-lived charge carriers using time-resolved microwave conductivity (TRMC) measurements (Supplementary Section 11). The carrier-decay dynamics show both a fast decay component (G$^{•+}$–NDI$^{•−}$, τ = 768 ns, and G$^{•+}$–PDI$^{•−}$, τ = 909 ns) and a significant signal that lives past the 8 µs time window of the experiment, consistent with the time-resolved transient-absorption results. The faster carrier-decay dynamics, after geminate recombination, are attributed to the equilibration between mobile and trapped carriers at defect sites, whereas the slower charge recombination and de-trap processes take place on the microsecond time scale[41,42]. During this period, both G-quadruplex frameworks maintain >40% of the initial TRMC intensity, which suggests a good carrier mobility that most probably results from the highly ordered stacking of π chromophores. Similarly, high electron mobility has been studied by TRMC in other π-stacked arrays of NDI chromophores[43]. Additional information on the nature of these carriers was obtained from TRMC measurements in the presence of oxygen, and is reported in Supplementary Section 11.

Radical anions in G-quadruplex frameworks. To obtain deeper insights into the mobile radical ions in the ordered G2NDI and G2PDI chromophore stacks, the materials were partially reduced by soaking the solids in a cobaltocene (CoCp$_2$) solution in CH$_2$Cl$_2$ (0.07 equiv.) to produce NDI$^{•−}$ or PDI$^{•−}$ in the respective frameworks. The continuous-wave EPR (CW-EPR) spectrum of partially reduced G2NDI (Fig. 5a) shows a very narrow linewidth and asymmetry resulting from g-factor anisotropy, compared with monomeric NDI$^{•−}$ in a polystyrene matrix. In monomeric NDI$^{•−}$, the broad linewidth results from unresolved hyperfine coupling to the four core ^{1}H and two imide ^{14}N nuclei, in addition to g-factor anisotropy. Assuming such g anisotropy is preserved in the G2NDI spectrum, it can be concluded that the narrowing of the G2NDI spectrum results from a reduction in the hyperfine

coupling as compared with monomeric NDI$^{•−}$. Such a linewidth reduction is well known for systems in which the unpaired electron is shared across multiple sites on the EPR timescale[28,44]. Norris et al. have shown that the linewidth of such a spectrum is √ proportional to 1/N, where N is the number of sites over which the spin is shared[44]. For G2NDI, the full-width at half-maximum (FWHM) of the integrated CW-EPR spectrum decreases from 0.86 to 0.46 mT, which corresponds to N ≅ 3.5. The unpaired electron is therefore shared over 3–4 NDI units. As this analysis neglects sources of broadening other than hyperfine coupling, it is possible that the unpaired electron is shared over a larger number of sites.

For G2PDI, substantial narrowing of the CW-EPR spectrum is also observed (Fig. 5b). The FWHM of the integrated CW-EPR spectrum decreases from 0.83 to 0.32 mT between PDI$^{•−}$ in the polystyrene matrix and the framework, which corresponds to N ≅ 6.7 as a lower bound for the number of PDI units over which the spin is shared. These results again suggest substantial electron mobility in G2NDI and G2PDI frameworks.

In aggregates of randomly oriented molecules, the electron sharing is expected to average the g anisotropy and results in isotropic spectra. Instead, the observation of an anisotropic g factor, especially pronounced for G2NDI, strongly suggests that the movement of the unpaired spin occurs over NDI units that are oriented in a particular direction relative to each other, rather than in a highly disordered array.

G2PDI as an organic cathode material in a Li-ion battery. The facile electron transport in G2PDI and its structural stability in highly polar solvents further suggest the potential of this material as an electron-storage medium in lithium-ion batteries[45,46]. Although they offer theoretically high energy density in batteries, organic cathodes face various challenges, such as high solubility of the redox-active species in electrolyte solutions, restricted electrolyte ion mobility and poor electrical conductivity, that inevitably hinder their development. The ordered PDI stacks should offer ideal conduits for electron conduction, as suggested by the optical and EPR experiments described above, and Li$^+$ ions should be able to be transported through the electrolytes in the porous framework, thus overcoming the aforementioned issues. Although Li$^+$ ions are often anticipated to associate closely with the carbonyl oxygens when organic imides are reduced at the cathode[47,48], the existence of the G-quadruplex moieties in G2PDI should additionally provide ion channels[49,50] for Li$^+$ diffusion as well as favourable locations for Li$^+$ to reside.

To test this hypothesis, coin-cell batteries that comprise G$_2$PDI as the organic cathode and metallic lithium as the anode were fabricated and characterized as given in Supplementary Section 12. The cyclic voltammogram (CV, $v = 0.5$ mV s^{-1}) of the G$_2$PDI battery dis-plays two reversible waves at about +1.9 and +2.3 V versus the Li$^+$/Li couple, which corresponds to the two redox steps that convert G$_2$PDI $\rightarrow^{e-}$ G$_2$PDI^{1-} $\rightarrow^{e-}$ G$_2$PDI^{2-} (Fig. 6a). Galvanostatic charge/discharge cycling measurements were performed at a current rate of 10 mA g^{-1} with a voltage range from 1.5 to 3 V. The voltage profile at the charging cycle, as shown in Supplementary Section 12, indicates two plateaus at about 1.8 and 2.3 V, which are consistent with the CV measurements. The specific discharge capacity of the G$_2$PDI cathode, as indicated in Fig. 6b, was 27 mAh g^{-1} at the first cycle, which corresponds to a 72% efficiency with respect to the theoretical value assuming each PDI can take-up two electrons. The capacity retention and coulombic efficiency shown in Fig. 6b imply that the G$_2$PDI framework is exceptionally stable. The capacity loss after 300 charge/discharge cycles is less than 7%, which corresponds to 99.97% of the capacity retention at each cycle. The high capacity-retention characteristics of the G$_2$PDI cathode are attributed to the stable framework structure that keeps the PDI species intact without letting them leach into the electrolyte. The first-cycle coulombic efficiency is about 92.5%, and the average coulombic efficiency of the latter cycles is above 99.6%, which indi-cates that the redox reactions at the PDI sites are highly reversible.

For comparison, we also used amorphous E$_2$PDI (Fig. 1) as a cathode material for the same electrochemical characterization (Supplementary Section 12). We observed that the E$_2$PDI-based battery has a substantially lower capacity retention, which is about 72.4% of the first cycle capacity after 300 charge/discharge cycles. The results evidently indicate that the well-defined framework structure of G$_2$PDI is essential for a better battery stability in the high-concentration electrolyte during repetitive electrochemical reactions.

Conclusions
Bioinspired crystalline organic frameworks using G-quadruplexes that serve as intrinsic electron donors linking planar aromatic electron acceptors were prepared. Photoexcitation of the ordered and segregated π-stacked NDI or PDI chromophores produces long-lived mobile charge carriers that are shared over several sites within the ordered architecture, a prerequisite for use in organic electronic devices. The structural stability and electrical conductivity of these frameworks were demonstrated by their application as cathode materials in a Li-ion battery. Further development of these materials towards optoelectronic applications will require the fabrication of thin films and quantitation of charge-carrier mobilities and yields. We envisage a wide range of functional materials that will display interesting optical, electronic, magnetic and catalytic properties can be assembled using the G-quadruplex strategy in addition to post-synthetic modifications of the frameworks.

Methods
General procedure for G-quadruplex framework preparation. The Boc-protected precursors (30 mg) were dissolved in a mixture of CH$_2$Cl$_2$ (4 ml) and TFA (1 ml) at room temperature in a capped 20 ml scintillation vial; the cap was opened once after 15 h to allow the generated CO$_2$ to escape. The vial was opened after 30–40 h and then placed in a closed chamber that contained MeOH (30 ml). Vapour exchange took place in this chamber for 24 h until G$_2$NDI or G$_2$PDI precipitated fully. The solids were collected by filtration under reduced pressure, and washed with CH$_2$Cl$_2$. For G$_2$PDI, the solids were soaked in warm DMF at 50 °C for five days to improve the crystallinity.

Computational construction of self-assembly structures. Hypothetical structures for the porous frameworks based on G$_2$NDI and G$_2$PDI were constructed in silico using the Crystal Builder and Forcite modules of Materials Studio. Simulated nitrogen isotherms in these structures were calculated using the simulation code RASPA.

Sample preparation for spectroscopic characterization. The instrumentation is detailed in the Supplementary Information. For both steady-state and transient optical measurements, solid G$_2$NDI or G$_2$PDI (0.3 mg) was sonicated in a solution of polyisobutylene (0.2 ml, ~10 mg ml^{-1}) in hexanes for 5–10 min, the suspension was dropcast onto a glass slide and the solvent was evaporated in vacuo. For diffuse reflectance infrared spectroscopy, the samples were ground and mixed in a KBr matrix.

Samples for PXRD measurements were loaded as dry powders into thin-walled glass capillary tubes (Charles-Supper, 0.7 mm outer diameter (o.d.)). Similarly, samples for TREPR and TRMC were loaded as dry powders into quartz tubes (1.80 mm o.d. × 1.50 mm inner diameter (i.d.)) and sealed under vacuum using an oxyhydrogen torch.

Chemically reduced framework samples for CW-EPR were prepared in an N$_2$ glovebox by adding a solution of CoCp$_2$ in CH$_2$Cl$_2$ (0.07 mol CoCp$_2$ per mol NDI or PDI) to a stirred suspension of the framework in CH$_2$Cl$_2$. The resulting reduced suspension was added to quartz tubes (1.80 mm o.d. × 1.50 mm i.d.) and allowed to settle. The tubes were sealed with ultraviolet-curing epoxy prior to removal from the glovebox. NDI and PDI anion standards in polystyrene were prepared in an N$_2$ glovebox by the addition of the CoCp$_2$ solution in CH$_2$Cl$_2$ to a THF solution of polystyrene. The solution was then dropcast onto glass slides and dried further under vacuum. The resulting polystyrene films were scraped off and loaded into quartz tubes (4.0 mm o.d. × 3.0 mm i.d.), which were affixed to a vacuum valve and unloaded from the glovebox. The tubes were evacuated (10^{-4} torr) and sealed under vacuum using an oxyhydrogen torch.

Fabrication of the Li-ion half-cell battery. Slurries were prepared by mixing the active materials (80 wt%) with conductive carbon black (Super-P, 10 wt%) and polyvinylidene fluoride (10 wt%) binder in anhydrous DMF and coated onto an aluminium foil substrate. These slurries were dried in a vacuum oven at 90 °C for 12 h, and subsequently used to fabricate batteries in a half-cell geometry with a lithium disc as the counter electrode. The electrolyte used was 1 M LiPF$_6$ in ethyl carbonate/dimethyl carbonate (1:1 v/v).

References
1. Coropceanu, V. et al. Charge transport in organic semiconductors. Chem. Rev. 107, 926–952 (2007).
2. Grozema, F. C. & Siebbeles, L. D. A. Mechanism of charge transport in self-organizing organic materials. Int. Rev. Phys. Chem. 27, 87–138 (2008).
3. Roznyatovskiy, V. V., Carmieli, R., Dyar, S. M., Brown, K. E. & Wasielewski, M. R. Photodriven charge separation and transport in self-assembled zinc tetrabenzotetraphenylporphyrin and perylenediimide charge conduits. Angew. Chem. Int. Ed. 53, 3457–3461 (2014).
4. Hartnett, P. E. et al. Long-lived charge carrier generation in ordered films of a covalent perylenediimide-diketopyrrolopyrrole-perylenediimide molecule. Chem. Sci. 6, 402–411 (2015).
5. Mallia, A. R., Salini, P. S. & Hariharan, M. Nonparallel stacks of donor and acceptor chromophores evade geminate charge recombination. J. Am. Chem. Soc. 137, 15604–15607 (2015).
6. Dogru, M. & Bein, T. On the road towards electroactive covalent organic frameworks. Chem. Commun. 50, 5531–5546 (2014).
7. Colson, J. W. & Dichtel, W. R. Rationally synthesized two-dimensional polymers. Nat. Chem. 5, 453–465 (2013).
8. Ding, S.-Y. & Wang, W. Covalent organic frameworks (COFs): from design to applications. Chem. Soc. Rev. 42, 548–568 (2013).
9. Waller, P. J., Gandara, F. & Yaghi, O. M. Chemistry of covalent organic frameworks. Acc. Chem. Res. 48, 3053–3063 (2015).
10. Wan, S., Guo, J., Kim, J., Ihee, H. & Jiang, D. A photoconductive covalent organic framework: self-condensed arene cubes composed of eclipsed 2D polypyrene sheets for photocurrent generation. Angew. Chem. Int. Ed. 48, 5439–5442 (2009).
11. Jin, S. B. et al. Charge dynamics in a donor−acceptor covalent organic framework with periodically ordered bicontinuous heterojunctions. Angew. Chem. Int. Ed. 52, 2017–2021 (2013).
12. Wan, S. et al. Covalent organic frameworks with high charge carrier mobility. Chem. Mater. 23, 4094–4097 (2011).
13. Ding, X. S. et al. Synthesis of metallophthalocyanine covalent organic frameworks that exhibit high carrier mobility and photoconductivity. Angew. Chem. Int. Ed. 50, 1289–1293 (2011).
14. Cai, S.-L. et al. Tunable electrical conductivity in oriented thin films of tetrathiafulvalene-based covalent organic framework. Chem. Sci. 5, 4693–4700 (2014).
15. Wilson, A. J. Non-covalent polymer assembly using arrays of hydrogen-bonds. Soft Matter 3, 409–425 (2007).
16. Chen, T.-H. et al. Thermally robust and porous noncovalent organic framework with high affinity for fluorocarbons and CFCs. Nat. Commun. 5, 5131 (2014).

17. Li, P. et al. A rod-packing microporous hydrogen-bonded organic framework for highly selective separation of C_2H_2/CO_2 at room temperature. Angew. Chem. Int. Ed. 54, 574–577 (2015).
18. He, Y. B., Xiang, S. C. & Chen, B. L. A microporous hydrogen-bonded organic framework for highly selective C_2H_2/C_2H_4 separation at ambient temperature. J. Am. Chem. Soc. 133, 14570–14573 (2011).
19. Wu, Y.-L., Brown, K. E. & Wasielewski, M. R. Extending photoinduced charge separation lifetimes by using supramolecular design: guanine–perylenediimide G-quadruplex. J. Am. Chem. Soc. 135, 13322–13325 (2013).
20. Wu, Y.-L., Brown, K. E., Gardner, D. M., Dyar, S. M. & Wasielewski, M. R. Photoinduced hole injection into a self-assembled π-extended G-quadruplex. J. Am. Chem. Soc. 137, 3981–3990 (2015).
21. Sessler, J. L., Sathiosatham, M., Doerr, K., Lynch, V. & Abboud, K. A. A G-quartet formed in the absence of a templating metal cation: a new 8-(N,N-dimethylaniline)guanosine derivative. Angew. Chem. Int. Ed. 39, 1300–1303 (2000).
22. Otero, R. et al. Guanine quartet networks stabilized by cooperative hydrogen bonds. Angew. Chem. Int. Ed. 44, 2270–2275 (2005).
23. Zambounis, J. S., Hao, Z. & Iqbal, A. Latent pigments activated by heat. Nature 388, 131–132 (1997).
24. Hartnett, P. E. et al. Slip-stacked perylenediimides as an alternative strategy for high efficiency nonfullerene acceptors in organic photovoltaics. J. Am. Chem. Soc. 136, 16345–16356 (2014).
25. Huang, N., Chen, X., Krishna, R. & Jiang, D. L. Two-dimensional covalent organic frameworks for carbon dioxide capture through channel-wall functionalization. Angew. Chem. Int. Ed. 54, 2986–2990 (2015).
26. Giorgi, T. et al. Gel-like lyomesophases formed in organic solvents by self-assembled guanine ribbons. Chem. Eur. J. 8, 2143–2152 (2002).
27. El Garah, M. et al. Guanosine-based hydrogen-bonded 2D scaffolds: metal-free formation of G-quartet and G-ribbon architectures at the solid/liquid interface. Chem. Commun. 51, 11677–11680 (2015).
28. Wu, Y. et al. Electron delocalization in a rigid cofacial naphthalene-1,8:4,5-bis (dicarboximide) dimer. Angew. Chem. Int. Ed. 53, 9476–9481 (2014).
29. McCarthy, B. D., Hontz, E. R., Yost, S. R., Van Voorhis, T. & Dinca, M. Charge transfer or J-coupling? Assignment of an unexpected red-shifted absorption band in a naphthalenediimide-based metal–organic framework. J. Phys. Chem. Lett. 4, 453–458 (2013).
30. Yushchenko, O. et al. Ultrafast intersystem-crossing dynamics and breakdown of the Kasha-Vavilov's rule of naphthalenediimides. J. Phys. Chem. Lett. 6, 2096–2100 (2015).
31. Bullock, J. E. et al. Photophysics and redox properties of rylene imide and diimide dyes alkylated ortho to the imide groups. J. Phys. Chem. B 114, 1794–1802 (2010).
32. Gosztola, D., Niemczyk, M. P., Svec, W., Lukas, A. S. & Wasielewski, M. R. Excited doublet states of electrochemically generated aromatic imide and diimide radical anions. J. Phys. Chem. A 104, 6545–6551 (2000).
33. Weller, A. Photoinduced electron-transfer in solution—exciplex and radical ion-pair formation free enthalpies and their solvent dependence. Z. Phys. Chem. 133, 93–98 (1982).
34. Credgington, D., Jamieson, F. C., Walker, B., Nguyen, T. Q. & Durrant, J. R. Quantification of geminate and non-geminate recombination losses within a solution-processed small-molecule bulk heterojunction solar cell. Adv. Mater. 24, 2135–2141 (2012).
35. Hodgkiss, J. M. et al. Subnanosecond geminate charge recombination in polymer–polymer photovoltaic devices. Phys. Rev. Lett. 104, 177701 (2010).
36. Wiederrecht, G. P., Svec, W. A. & Wasielewski, M. R. Triplet states with unusual spin polarization resulting from radical ion pair recombination at short distances. J. Am. Chem. Soc. 121, 7726–7727 (1999).
37. Bullock, J. E., Carmieli, R., Mickley, S. M., Vura-Weis, J. & Wasielewski, M. R. Photoinitiated charge transport through π-stacked electron conduits in supramolecular ordered assemblies of donor–acceptor triads. J. Am. Chem. Soc. 131, 11919–11929 (2009).
38. Closs, G. L., Forbes, M. D. E. & Norris, J. R. Spin-polarized electron-paramagnetic resonance-spectra of radical pairs in micelles—observation of electron spin–spin interactions. J. Phys. Chem. 91, 3592–3599 (1987).
39. Kobori, Y., Sekiguchi, S., Akiyama, K. & Tero-Kubota, S. Chemically induced dynamic electron polarization study on the mechanism of exchange interaction in radical ion pairs generated by photoinduced electron transfer reactions. J. Phys. Chem. A 103, 5416–5424 (1999).
40. Trifunac, A. D., Nelson, D. J. & Mottley, C. Chemically induced dynamic electron polarization. Examples of $S-T_{\pm 1}$ polarization. J. Magn. Reson. 30, 263–272 (1978).
41. Nardes, A. M. et al. Photoinduced charge carrier generation and decay in sequentially deposited polymer/fullerene layers: bulk heterojunction vs planar interface. J. Phys. Chem. C 116, 7293–7305 (2012).
42. Ferguson, A. J., Kopidakis, N., Shaheen, S. E. & Rumbles, G. Dark carriers, trapping, and activation control of carrier recombination in neat P3HT and P3HT:PCBM blends. J. Phys. Chem. C 115, 23134–23148 (2011).
43. Mondal, T., Sakurai, T., Yoneda, S., Seki, S. & Ghosh, S. Semiconducting nanotubes by intrachain folding following macroscopic assembly of a naphthalene–diimide (NDI) appended polyurethane. Macromolecules 48, 879–888 (2015).
44. Norris, J. R., Uphaus, R. A., Crespi, H. L. & Katz, J. Electron spin resonance of chlorophyll and origin of signal-I in photosynthesis. Proc. Natl Acad. Sci. USA 68, 625–628 (1971).
45. Song, Z. & Zhou, H. Towards sustainable and versatile energy storage devices: an overview of organic electrode materials. Energy Environ. Sci. 6, 2280–2301 (2013).
46. Liang, Y., Tao, Z. & Chen, J. Organic electrode materials for rechargeable lithium batteries. Adv. Ener. Mater. 2, 742–769 (2012).
47. Song, Z., Zhan, H. & Zhou, Y. Polyimides: promising energy-storage materials. Angew. Chem. Int. Ed. 49, 8444–8448 (2010).
48. Xu, F. et al. Electrochemically active, crystalline, mesoporous covalent organic frameworks on carbon nanotubes for synergistic lithium-ion battery energy storage. Sci. Rep. 5, 8225 (2015).
49. Forman, S. L., Fettinger, J. C., Pieraccini, S., Gottareli, G. & Davis, J. T. Toward artificial ion channels: a lipophilic G-quadruplex. J. Am. Chem. Soc. 122, 4060–4067 (2000).
50. Arnal-Herault, C. et al. Functional G-quartet macroscopic membrane films. Angew. Chem. Int. Ed. 46, 8409–8413 (2007).

Acknowledgements

Author contributions

Y.-L.W. and M.R.W. planned and directed the project. Y.-L.W., N.E.H., N.S.L., K.-S.C., L.M, and T.C.W. prepared the materials, performed the structural characterization and carried out measurements and data analysis. D.A.G.-G. developed the structural models and carried out the simulations. All the authors contributed to the analysis of the results and the writing of the manuscript.

Additional information

Competing financial interests